Extremal-point density of scaling processes: From fractional Brownian motion to turbulence in one dimension

Yongxiang Huang (黄永祥),[1,*] Lipo Wang (王利坡),[2] F. G. Schmitt,[3] Xiaobo Zheng (郑小波),[4] Nan Jiang (姜楠),[4] and Yulu Liu (刘宇陆)[5]

[1]*State Key Laboratory of Marine Environmental Science, College of Ocean and Earth Sciences, Xiamen University, Xiamen 361102, China*

[2]*UM-SJTU Joint Institute, Shanghai JiaoTong University, Shanghai, 200240, China*

[3]*CNRS, Univ. Lille, Univ. Littoral Cote d'Opale, UMR 8187, LOG, Laboratoire d'Océanologie et de Géosciences, F 62 930 Wimereux, France*

[4]*Department of Mechanics, Tianjin University, 300072 Tianjin, China*

[5]*Shanghai Institute of Applied Mathematics and Mechanics, Shanghai University, Shanghai 200072, China*

(Received 7 February 2017; revised manuscript received 19 May 2017; published 17 July 2017)

In recent years several local extrema-based methodologies have been proposed to investigate either the nonlinear or the nonstationary time series for scaling analysis. In the present work, we study systematically the distribution of the local extrema for both synthesized scaling processes and turbulent velocity data from experiments. The results show that for the fractional Brownian motion (fBm) without intermittency correction the measured extremal-point-density (EPD) agrees well with a theoretical prediction. For a multifractal random walk (MRW) with the lognormal statistics, the measured EPD is independent of the intermittency parameter μ, suggesting that the intermittency correction does not change the distribution of extremal points but changes the amplitude. By introducing a coarse-grained operator, the power-law behavior of these scaling processes is then revealed via the measured EPD for different scales. For fBm the scaling exponent $\xi(H)$ is found to be $\xi(H) = H$, where H is Hurst number, while for MRW $\xi(\mu)$ shows a linear relation with the intermittency parameter μ. Such EPD approach is further applied to the turbulent velocity data obtained from a wind tunnel flow experiment with the Taylor scale λ-based Reynolds number $\mathrm{Re}_\lambda = 720$, and a turbulent boundary layer with the momentum thickness θ based Reynolds number $\mathrm{Re}_\theta = 810$. A scaling exponent $\xi \simeq 0.37$ is retrieved for the former case. For the latter one, the measured EPD shows clearly four regimes, which agrees well with the corresponding sublayer structures inside the turbulent boundary layer.

DOI: 10.1103/PhysRevE.96.012215

I. INTRODUCTION

Multiscale statistics is recognized as one of the most import features of complex dynamical systems. Several methodologies have been put forward to characterize the multiscale property, such as structure function analysis proposed by Kolmogorov [1], wavelet-based approaches [2,3], the Hilbert-Huang transform [4,5], and multilevel segment analysis [6]. The local extremal point (see definition below) plays important roles in multiscale characterization [2,4–6]. For example, in the Hilbert-Huang transform, local extrema are used to construct the upper and lower envelope [4]; in multilevel segment analysis, a structure function is defined conditionally on the segments between consecutive extremal points [6]. Experimental results suggest that these two methods can overcome some potential shortcomings of the conventional structure function [6–8], such as scale mixing. The scale and the corresponding scaling or multifractal nature are embedded in the local extremal point statistics, which definitely deserves further studies.

The distribution of local extremal points is associated with the dynamical behavior of the considered process. For a discrete time series $x(t_i)$, $i = 1,2,3\ldots N$, and a sampling frequency f_s, the local extremal point (either local maxima or minima) satisfies the following relation:

$$x_t(t_{i+1})x_t(t_i) < 0, \tag{1}$$

where $x_t(t_i) = [x(t_{i+1}) - x(t_i)]/(t_{i+1} - t_i)$ is the local slope of $x(t_i)$. This property is used for direct counting of the number of extrema. Clearly the local extrema correspond to the zero-crossing of the first-order derivative of $x(t_i)$. If $x(t_i)$ acts as the turbulent velocity, $x_t(t_i)$ is then the acceleration. The local extreme is thus an indicator of the sign change of the acceleration and forcing, showing the dynamical property of $x(t_i)$ [6]. Theoretically, Rice [9] proved that for a stationary continuous process $x(t)$, if $x(t)$ and $x_t(t)$ are statistically independent and Gaussian distributed, then the zero-crossing ratio (ZCR) per second of $x(t)$, denoted as N_0, can be expressed as

$$N_0 = \frac{1}{\pi}\left(\frac{\langle x_t^2(t)\rangle_t}{\langle x^2(t)\rangle_t}\right)^{1/2}, \tag{2}$$

where $\langle\,\rangle_t$ means the sample average with respect to t.

Similarly, ZCR of the first-order derivative, i.e., $x_t(t)$, denoted as N_1 can be written as [11]

$$N_1 = \frac{1}{\pi}\left(\frac{\langle x_{tt}^2(t)\rangle_t}{\langle x_t^2(t)\rangle_t}\right)^{1/2}, \tag{3}$$

where $x_{tt}(t)$ is the second-order derivative. The corresponding extremal-point-density (EPD), e.g., the ratio between number of extremal points and the total data length, is then written as

$$\mathcal{I} = \frac{N_1}{f_s} = \frac{1}{\pi f_s}\left(\frac{\langle x_{tt}^2(t)\rangle_t}{\langle x_t^2(t)\rangle_t}\right)^{1/2}, \tag{4}$$

where f_s is the sampling frequency of the discrete process. Later, Ylvisaker [12] showed that in Eq. (2) for any continuous

*yongxianghuang@gmail.com

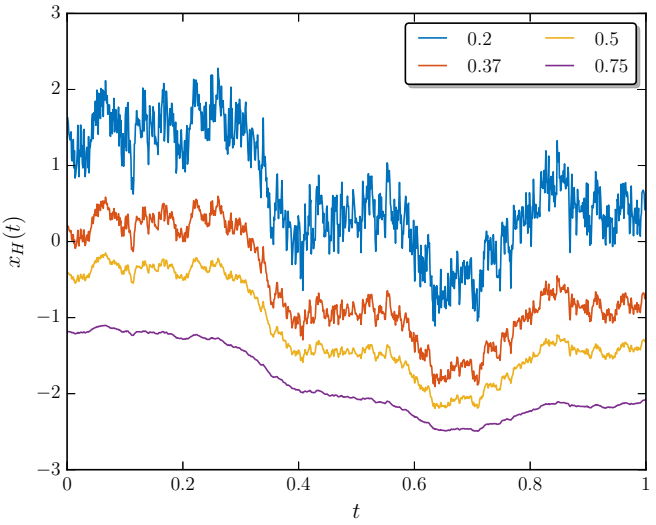

FIG. 1. Synthesized fractional Brownian motion data for various Hurst number H using the same random numbers in the Wood-Chan algorithm with 1024 data points in each realization. Visually, with the increasing of H, the fBm curve becomes more and more smooth, i.e., has less extremal points. For display clarity, these curves have been vertically shifted.

stationary Gaussian process with finite N_0 the statistical independence between $x(t_i)$ and $x_t(t_i)$ need not to be involved. More details about ZRC and the Rice formula can be found in Ref. [10].

Toroczkai *et al.* [13] proposed another theory to estimate EPD as follows. Assume that $p(\phi_1,\phi_2)$, the joint probability density function (pdf) of the distribution of two neighbor slopes ϕ_1 and ϕ_2 with $\phi_i = x(t_{i+1}) - x(t_i)$, satisfies a joint Gaussian distribution as

$$p(\phi_1,\phi_2) = \frac{1}{2\pi\sqrt{D}} \exp\left[-\frac{d}{2D}\left(\phi_1^2 + \phi_2^2 - 2\frac{c}{d}\phi_1\phi_2\right)\right], \tag{5}$$

where $\langle\phi_1^2\rangle = \langle\phi_2^2\rangle = d > 0$, $\langle\phi_1\phi_2\rangle = c$, and $D = d^2 - c^2 > 0$. Then the process EPD $\mathcal{I} = N_e/N$, where N_e and N are, respectively, the number of extremal points and the data length, is determined by

$$\mathcal{I} = \frac{1}{\pi}\arccos\left(\frac{\langle\phi_1\phi_2\rangle}{\langle\phi_1^2\rangle}\right) = \frac{1}{\pi}\arccos\left(\frac{c}{d}\right). \tag{6}$$

For more details of this theory the reader is referred to Ref. [13].

Specifically for the turbulent velocity, Liepmann [14] pointed out theoretically that ZRC can be related with the Taylor microscale λ via the following relation:

$$\lambda = \frac{1}{\pi N_0}, \tag{7}$$

which has been verified experimentally [15,16]. In the turbulence literature, the local extrema or zero-crossing or level-crossing are also related with the dissipation scale or

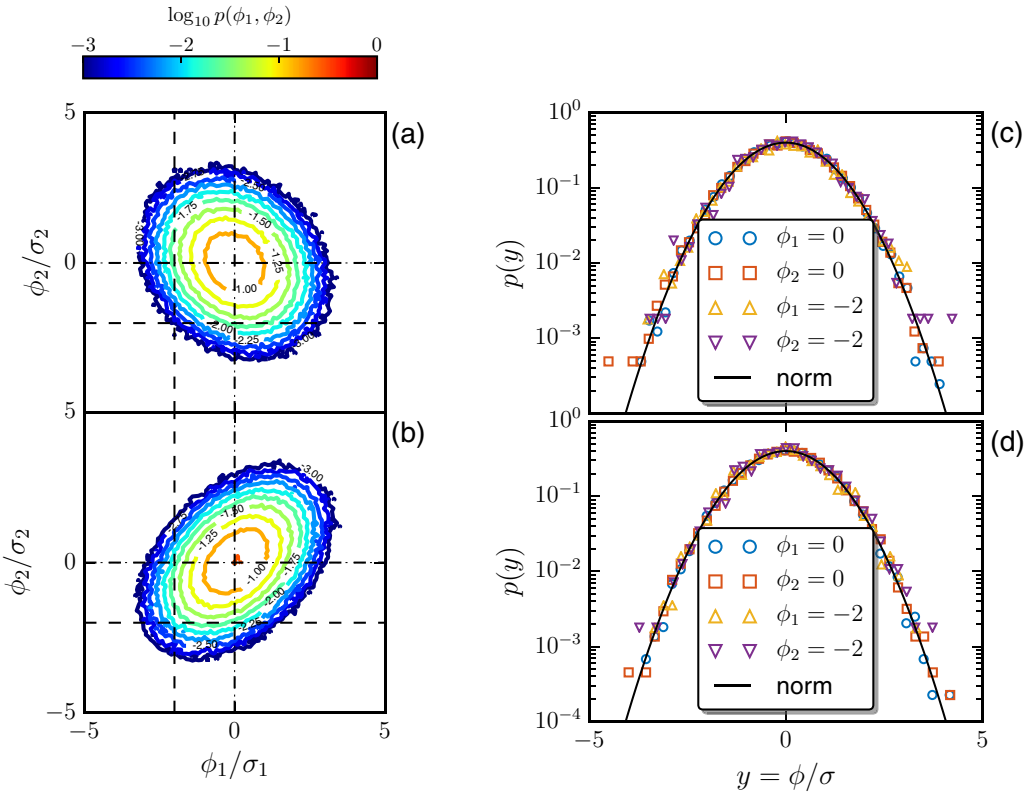

FIG. 2. Joint pdf $p(\phi_1,\phi_2)$ for (a) $H = 1/3$ and (b) $H = 0.75$. The corresponding normalized conditional pdf $p(y)$ at various ϕ_1 and ϕ_2 for (c) $H = 1/3$ and (d) $H = 0.75$. For comparison, the normal distribution is illustrated as a solid line. Dashed lines in (a) and (b) denote the calculated ϕ_1 and ϕ_2 value.

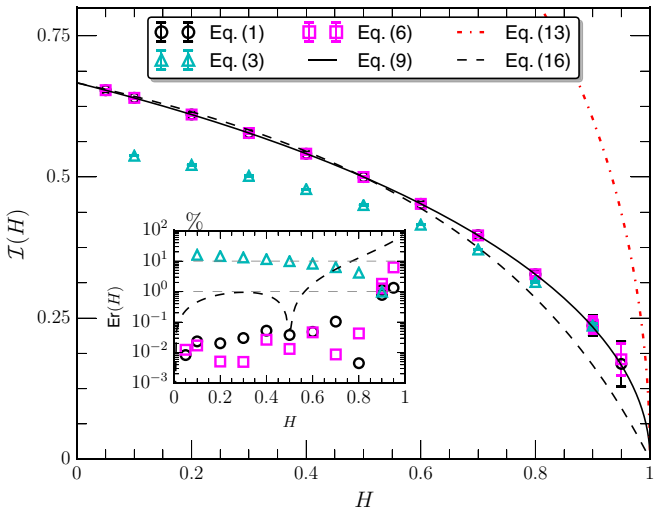

FIG. 3. Comparison of the measured $\mathcal{I}(H)$ from direct counting, Eq. (1) (◯), Eq. (6) (□) via calculating ϕ_i and Eq. (4) via calculating $\langle x_t(t_i)^2\rangle$ and $\langle x_{tt}(t_i)^2\rangle$ (△), with theoretical predictions by Eqs. (9) (solid line: $\frac{1}{\pi}\arccos(2^{2H-1}-1)$), (13) (dashed-dotted line: $2\sqrt{\frac{2-2H}{4-2H}}$), and (16) (dashed line: $\frac{2-2H}{3-2H}$), respectively. The inset shows the relative errors between Eq. (9) and others.

intermittency [17–21]. For example, Ho and Zohar [17] proposed a peak-valley-counting technique to detect the dissipation scale and found that the most probable scale equals the wavelength at the peak of the dissipation spectrum. Yang *et al.* [21] studied the local zero-crossings and their relation with inertial range intermittency for the transverse velocity and passive scalar in an incompressible isotropic turbulent field. They demonstrated that the most intermittent regions for the transverse velocity are inclined to be vortex dominated.

In this paper, the statistics of EPD of several representative scaling processes will be investigated. We first verify Eqs. (4) and (6) using synthesized fractional Brownian motion (fBm) and multifractal random walk (MRW) in Sec. II. A coarse-grained algorithm is then proposed to detect the respective scaling behavior. In Sec. III, the real data obtained from various typical turbulent flows are analyzed and the main conclusions are summarized in Sec. IV.

II. NUMERICAL VALIDATION

A. Fractional Brownian motion

1. *Extremal-point-density of fractional Brownian motion*

First fBm is considered here as a toy model for a better understanding of the Hurst-dependence of EPD. As a generalization of the classical Brownian motion, fBm was introduced by Kolmogorov [22] and extensively studied by Mandelbrot and coworkers in the 1960s [23]. Since then, fBm became a classical monoscaling stochastic process in many fields [24–26]. Its first-order derivative is the so-called fractional Gaussian noise (fGn) with the covariance as

$$\rho_H(\tau) = \langle x'(t)x'(t+\tau)\rangle_t = \frac{\sigma^2}{2}(|\tau-1|^{2H} - 2|\tau|^{2H} + |\tau+1|^{2H}), \quad (8)$$

where τ is the separation lag, $\rho_H(0)=\sigma^2$ is the variance, and H is the Hurst number. Accordingly, it yields $\langle\phi_1\phi_2\rangle = \rho_H(1) = \sigma^2(2^{2H-1}-1)$ and $\langle\phi_1^2\rangle = \rho_H(0) = \sigma^2$. Thus, from Eq. (6) the process EPD can be written as

$$\mathcal{I}(H) = \frac{1}{\pi}\arccos(2^{2H-1}-1). \quad (9)$$

Clearly, Eq. (9) satisfies the requirement $\mathcal{I}(1/2)=1/2$ and $\mathcal{I}(H)|_{\lim_{H\to1}}=0$; meanwhile, it predicts $\mathcal{I}(H)|_{\lim_{H\to0}}=2/3$.

As aforementioned, EPD of $x(t)$ can be associated with ZCR of $x'(t)$. We introduce here a nth-order spectral moment $\omega(n)$ for the fGn as

$$\omega(n) = \int_0^{f_s} E_H(f) f^n \, df, \quad (10)$$

where f_s is the sampling frequency of the considered discrete time series. EPD can be related with $E_H(f)$ via the following exact relation [9], i.e.,

$$\mathcal{I}(H) = \frac{2}{f_s}\times\sqrt{\frac{\omega(2)}{\omega(0)}}, \quad (11)$$

because for fGn,

$$E_H(f) \propto f^{1-2H}, \quad (12)$$

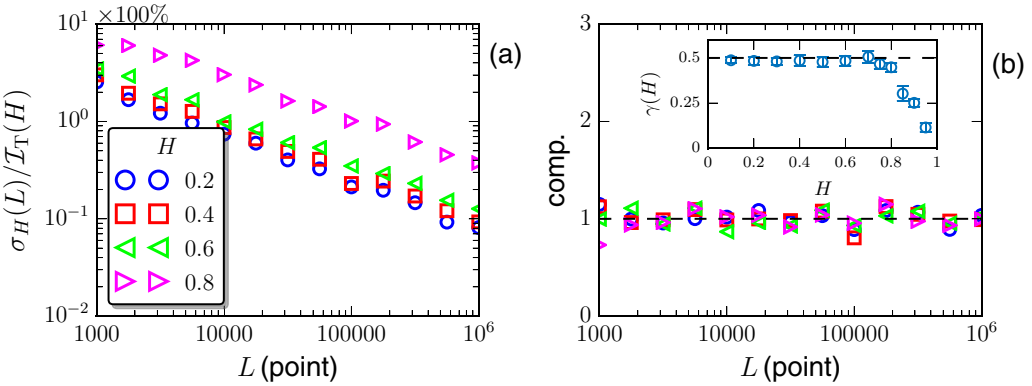

FIG. 4. (a) Relative standard deviation $\sigma_H(L)/\mathcal{I}_T(H)\times100\%$ for various H. (b) The compensated data using fitted parameters to emphasize the power-law behavior. The inset shows the measured scaling exponent $\gamma(H)$, where the dashed line shows the value 1/2, expected from the central limit theorem. The error bar is the 95% fitting confidence interval.

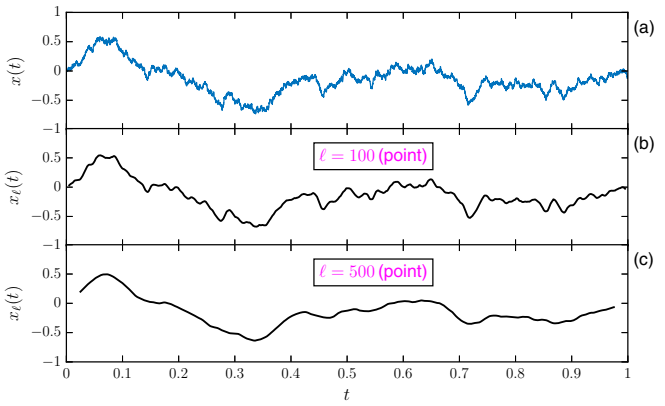

FIG. 5. Illustration of the filtering effect: (a) raw data with $H = 0.5$ and 10,000 data points; (b) $\ell = 100$ data points; (c) $\ell = 500$ data points. Increasing ℓ removes more local extremal points.

substituting Eq. (12) into Eq. (11) then yields

$$\mathcal{I}(H) = 2 \times \sqrt{\frac{2-2H}{4-2H}}. \tag{13}$$

It satisfies $\mathcal{I}(H)|_{\lim_{H\to 1}} = 0$; meanwhile, it predicts $\mathcal{I}(H)|_{\lim_{H\to 0}} = \sqrt{2}$ and $\mathcal{I}(1/2) = \sqrt{4/3}$, which is not consistent with the requirement $\mathcal{I} \leqslant 1$.

An energy weighted mean frequency can be defined as [4,27]

$$\tilde{f}(H) = \frac{\omega(1)}{\omega(0)}. \tag{14}$$

Together with Eqs. (10) and (12), one obtains

$$\tilde{f}(H) = f_s \times \frac{2-2H}{3-2H}. \tag{15}$$

Phenomenologically, we assume here that EPD of fBm can be related with the mean frequency $\tilde{f}(H)$ as

$$\mathcal{I}(H) = \frac{\tilde{f}(H)}{f_s} = \frac{2-2H}{3-2H}. \tag{16}$$

Note that both Eqs. (9) and (16) satisfy the requirements $\mathcal{I}(1/2) = 1/2$ and $\mathcal{I}(H)|_{\lim H\to 1} = 0$. Moreover, the limit case $\mathcal{I}(H)|_{\lim H\to 0} = 2/3$ can also be predicted, while Eq. (13) only satisfies the limit case $H \to 1$.

Numerically, a Fourier-based Wood-Chan algorithm [28] was used to generate the fBm data in the range $0 \leqslant H \leqslant 1$ for 100 realizations, each of which having the data length of L. Figure 1 shows the synthesized fBm data for various H with $L = 1024$ data points. For display clarity, the fBm curves have been vertically shifted. It needs to be mentioned that here for each realization the different H cases used the same random numbers in the algorithm for a detailed comparison. Visually, the larger H is, the smoother the process; or in other words, $\mathcal{I}(H)$ decreases with H.

Figure 2 shows the contour line of measured joint pdf $p(\phi_1,\phi_2)$ for (a) Hurst number $H = 1/3$ and (b) $H = 0.75$, respectively, with data length $L = 100\,000$ points. As indicated by Eq. (5), the inclined elliptic contour lines are centered at [0,0]. Several conditional pdfs $p(\phi_1|\phi_2)$ [or $p(\phi_2|\phi_1)$] at various ϕ_1 and ϕ_2 are shown in Figs. 2(c) and 2(d), where the solid line represents the normal distribution. The satisfactory agreement indicates the applicability of Toroczkai *et al.* [13]'s theory.

Figure 3 shows $\mathcal{I}(H)$ obtained from direct counting (Eq. (1), ◯), Eq. (4) by calculating $\langle x_t(t_i)^2\rangle$ and $\langle x_{tt}(t_i)^2\rangle$ (△), Eq. (6) by estimating ϕ_i (□), and theoretical predictions by Eq. (9) (solid line), Eq. (13) (dashed dotted line), and Eq. (16) (dashed line), respectively. The error bar is the standard deviation from 100 realizations. The direct measured $\mathcal{I}(H)$ (◯) agrees well with Eq. (9) but deviates from Eq. (16) when $H \geqslant 0.6$. Note that both the estimator by Eq. (4) and theoretical Eq. (13) are far from the direct measurement. The discrepancy of Rice's formula and the measurement might be due to the fact that the fBm process is not differentiable.

Since $\mathcal{I}_T(H)$ provided by Eq. (9) agrees very well with the direct counting results from Eq. (1), to characterize the measurement error, we introduce here the following relative error by taking Eq. (9) as the reference case,

$$\mathrm{Er}(H) = \frac{|\mathcal{I}(H) - \mathcal{I}_T(H)|}{\mathcal{I}_T(H)} \times 100\%, \tag{17}$$

which is presented in the inset in Fig. 3, where 1% and 10% are illustrated by a dashed line. For most of the values of H, $\mathrm{Er}(H)$ is less than 1%. Equation (16) has a $\leqslant$1% relative error when

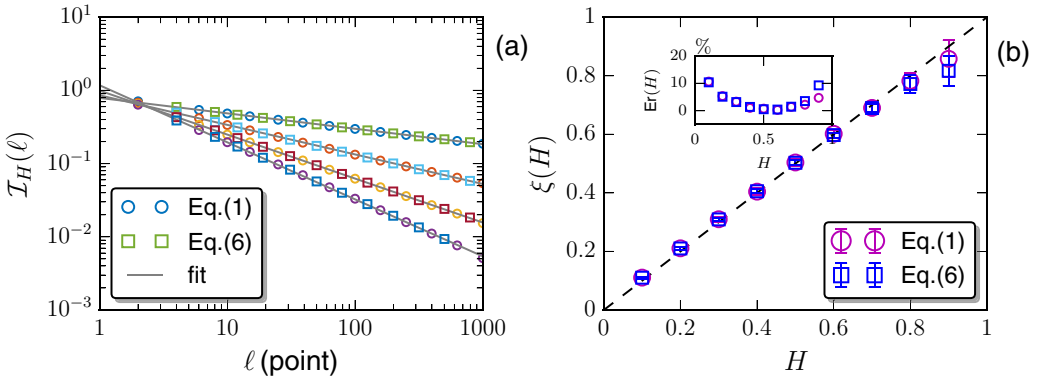

FIG. 6. (a) Measured $\mathcal{I}(H,\ell)$ with $H = 0.2$, 0.4, 0.6, and 0.8. The solid line is a power-law fit. For display convenience, $\mathcal{I}(H,\ell)$ is normalized by $\mathcal{I}(H,0)$. (b) The measured scaling exponent $\xi(H)$ versus H. The error bar is the standard deviation obtained from 100 realizations. The inset shows the relative error $\mathrm{Er}(H)$ versus H.

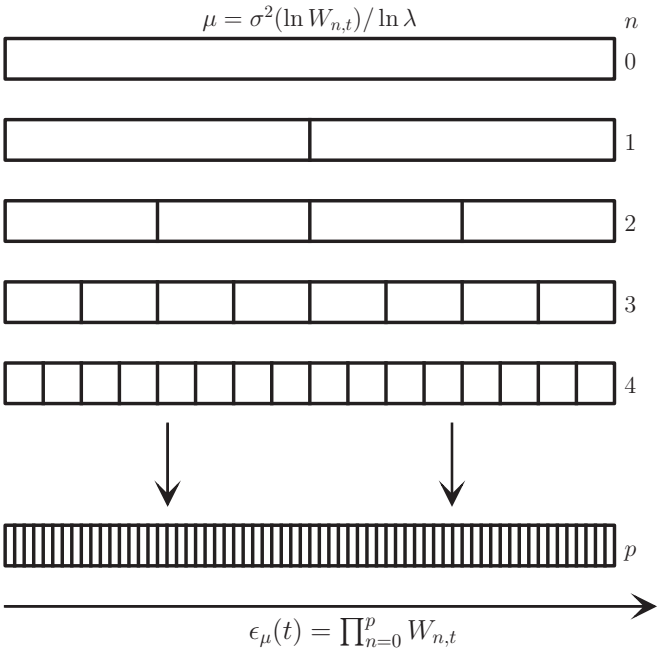

FIG. 7. Illustration of the discrete MRW cascade process. Each step is associated with a scale ratio of 2. After p steps, the total scale ratio is 2^p. The synthesized multifractal measure $\epsilon_\mu(t)$ has a lognormal statistics. The corresponding intermittency correction is controlled by the parameter $\mu = \sigma^2(\ln W_n)/\ln\lambda$.

$H \leqslant 0.6$, and a $\leqslant 10\%$ error when $H \leqslant 0.8$. Probably such deviation could result from the violation of the convergence assumption that is used to obtain Eq. (10).

2. *Finite-length effect*

To consider the influences of the finite length L, the synthesized fBm data were generated with different L in the range $10^3 \sim 10^6$, EPD is calculated only via the direct counting method. Figure 4(a) shows the measured relative standard deviation $\sigma_H(L)/\mathcal{I}_T(H) \times 100\%$ from 100 realizations, where $\mathcal{I}_T(H)$ is the prediction by Eq. (9). A power-law decay is observed for all H as

$$\sigma_H(L) \propto L^{-\gamma(H)}. \tag{18}$$

To emphasize such behavior, the corresponding compensated curves using data fitting are shown in Fig. 4(b), where the inset shows the measured scaling exponent $\gamma(H)$. A clear plateau confirms that the measured $\mathcal{I}(H)$ converges to the theoretical value with a power-law rate. It is interesting to note that when $H \leqslant 0.7$ the measured $\gamma(H)$ is about $1/2$, which can be expected theoretically from the central limit theorem. When $L \geqslant 10\,000$ data points, the relative error can be well controlled below 1% for $H \leqslant 0.7$.

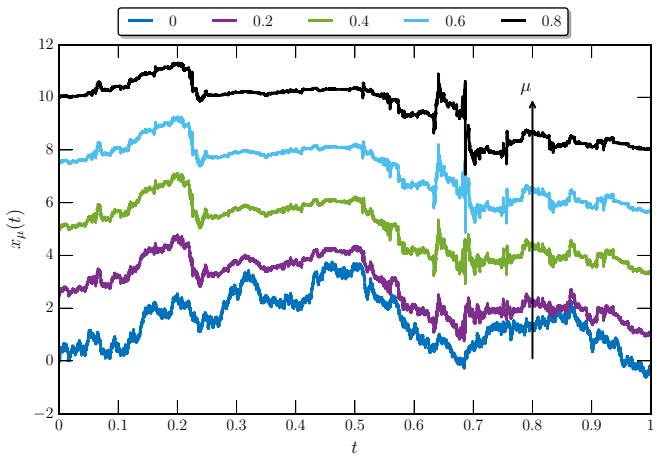

FIG. 8. Illustration of the synthesized MRW $x_\mu(t)$, for one realization with various intermittency parameter μ. For display clarity, the curves have been vertical shifted. The measured $\mathcal{I}(\mu) \simeq 0.5011$ is independent of μ since the same random number are used to construct the multifractal measure $\epsilon_\mu(t)$.

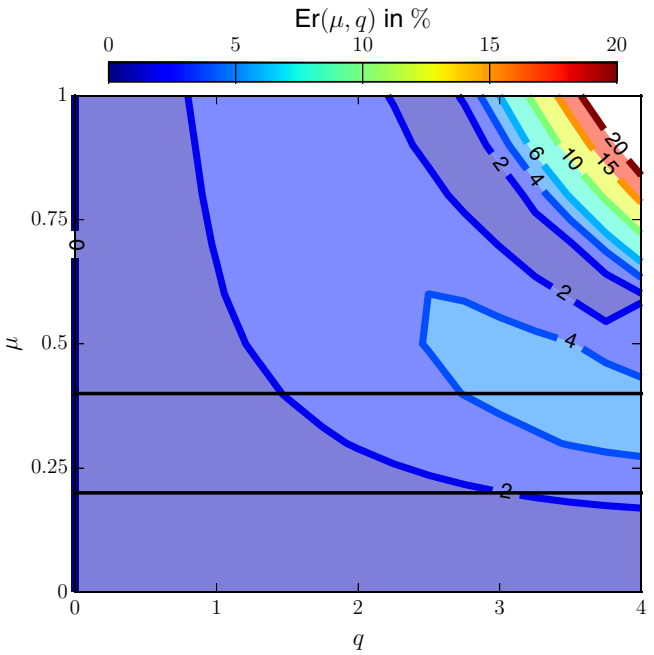

FIG. 9. Contour plot of the measured relative error between the structure function scaling exponent $\zeta(q)$ and the lognormal prediction by Eq. (26). The typical value $0.2 \leqslant \mu \leqslant 0.4$ for the Eulerian turbulent velocity is indicated by a horizontal solid line.

3. *Coarse-grained effect*

For the data from the real world, extremal points can be largely contaminated by noise from different sources. The low-pass filter technique is a commonly adopted remedy for such a problem. In the turbulence community the similar coarse-grained idea plays an important role in multifractal analysis, for instance, when considering the energy dissipation rate along the Lagrangian trajectory [29]. For a continuous process, e.g., $x(t)$, the coarse-grained variable is defined as

$$x_\ell(t) = \frac{1}{M}\int_{0\leqslant t\leqslant \ell} x(t+t')G(t')\,dt', \tag{19}$$

in which ℓ is the coarse-grained scale and $G(t')$ is the filtering kernel, and $M = \int_{0\leqslant t'\ell} G(t')\,dt'$. A simple choice is the hat

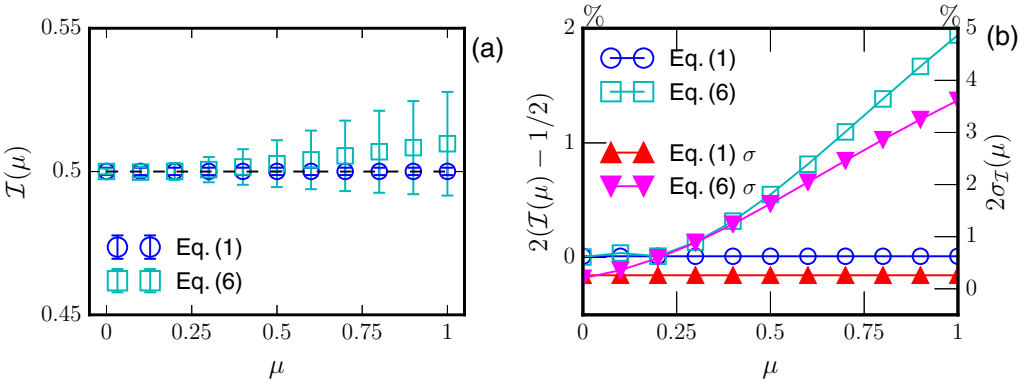

FIG. 10. (a) Measured EPD $\mathcal{I}(\mu)$ for MRW. The errorbar is the standard deviation from 100 realizations. Due to the intermittency effect, Eq. (6) overestimates $\mathcal{I}(\mu)$. (b) The relative error $\mathrm{Er}(\mu)$ for the measured $\mathcal{I}(\mu)$ (open symbols) and the standard deviation σ (closed symbols), where a theoretical value $\mathcal{I}(\mu) = 1/2$ is considered as the reference case.

function as

$$G(t') = \begin{cases} 1, & 0 \leqslant t' \leqslant \ell \\ 0, & \text{others.} \end{cases} \tag{20}$$

A discrete version of Eq. (19) is written as

$$x_\ell(t_i) = \frac{1}{M} \sum_{j=0}^{\ell-1} x(t_i + j) G(j), \tag{21}$$

where $M = \sum_{j=0}^{\ell-1} G(j)$ and ℓ is the coarse-grained scale.

Figure 5 illustrates an example of the filtering effect for $H = 1/2$ with 10 000 data points, where the number of local extrema decreases with the coarse-grained scale ℓ. Figure 6(a) shows with 100 realizations the coarse-grained $\mathcal{I}(H,\ell)$ with $1 \leqslant \ell \leqslant 1000$ from direct counting (◯) and Eq. (6), where the dependence of the correlation coefficients in Eq. (6) on ℓ can be obtained either numerically or theoretically.

For display convenience, $\mathcal{I}(H,\ell)$ has been normalized by $\mathcal{I}(H,0)$. Visually, Eq. (6) provides the same value as direct counting, since the joint pdf $p(\phi_1,\phi_2)$ can be well described by the joint Gaussian distribution, i.e., Eq. (5). The following power-law behavior is observed:

$$\mathcal{I}(H,\ell) \propto \ell^{-\xi(H)}. \tag{22}$$

Fig. 6(b) suggests that the scaling exponent $\xi(H) = H$, with the errorbars estimated as the standard deviation from 100 realizations. The inset shows the relative error $\mathrm{Er}(H)$ between $\xi(H)$ and H. Clearly $\mathrm{Er}(H)$ is less than 10%, implying a rather good estimation of the Hurst number H. Clearly, $\mathrm{Er}(H)$ is less than 10%, implying a rather good estimation of the Hurst number H.

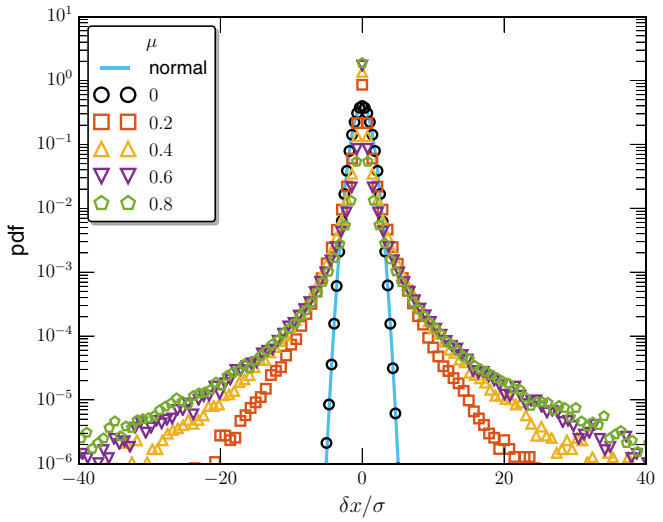

FIG. 11. Experimental pdfs for the first-order derivative of MRW, $\delta x = x'_\mu(t)$, with various μ. For display clarity, the pdfs have been normalized by their respective standard deviation.

B. Multifractal random walk with lognormal statistics

1. *Multifractal random walk with a discrete cascade*

Another important case to detect the influence from the intermittency correction is MRW with lognormal statistics, which is defined as

$$x_\mu(t) = \int_0^t \epsilon_\mu(t')^{1/2}\, dB(t'), \tag{23}$$

Here, $\epsilon_\mu(t)$ is a multifractal measure with lognormal statistics to provide an intermittency correction μ, and $B(t)$ is the Brownian motion to provide the scaling of the final process $x_\mu(t)$ [7,30–32]. Figure 7 illustrates the cascade process algorithm. The large scale corresponds to a unique cell of size $L = \ell_0 \lambda^p$, where ℓ_0 is a fixed scale and $\lambda > 1$ is the scale ratio, which for discrete models is typically set as $\lambda = 2$. The next level subscale corresponds to λ cells, each of which having the size $L/\lambda = \ell_0 \lambda^{p-1}$. Such scale cascade process continues from step $(1,2,\ldots)$ till p, leading to λ^p cells in total with the size of $L/\lambda^p = \ell_0$, which is the smallest scale of the cascade. Finally, the multifractal measure is written as the product of p random variables as follows:

$$\epsilon_\mu(t) = \prod_{n=0}^{p} W_{n,t}, \tag{24}$$

where $W_{n,t}$ is the lognormal random variable with independent identically distribution (i.i.d) corresponding to the position t and level n. In the cascade, $W_{n,t}$ has a mean value $\langle \ln W_{n,t} \rangle = -\frac{1}{2}\mu \ln \lambda$ and variance $\sigma^2(\ln W_n) = \mu \ln \lambda$, where μ controls the process intermittency [32].

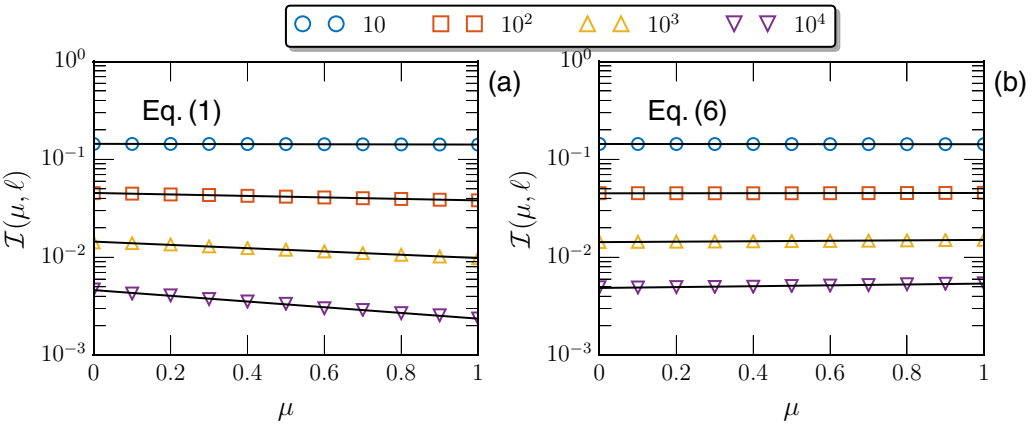

FIG. 12. Measured $\mathcal{I}(\mu,\ell)$ versus μ at various scale ℓ from (a) direct counting by Eq. (1), (b) Eq. (6). The solid line is an exponential fitting. Exponential-law is observed for both approaches, but with different trends.

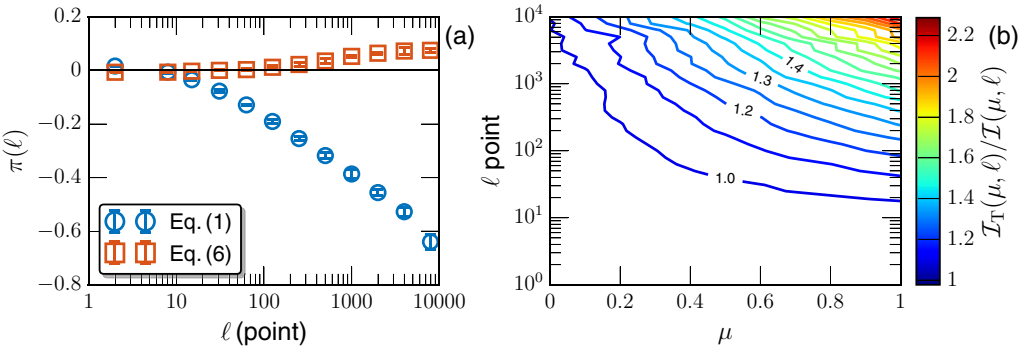

FIG. 13. (a) Experimental scaling exponent $\pi(\ell)$ versus ℓ. Due to the violation of the joint Gaussian distribution requirement, Eq. (6) fails to measure $\pi(\ell)$. (b) Contour plot of the measured ratio $\mathcal{I}_T(\mu,\ell)/\mathcal{I}(\mu,\ell)$ to confirm the overestimation of $\mathcal{I}(\mu,\ell)$ by Eq. (6).

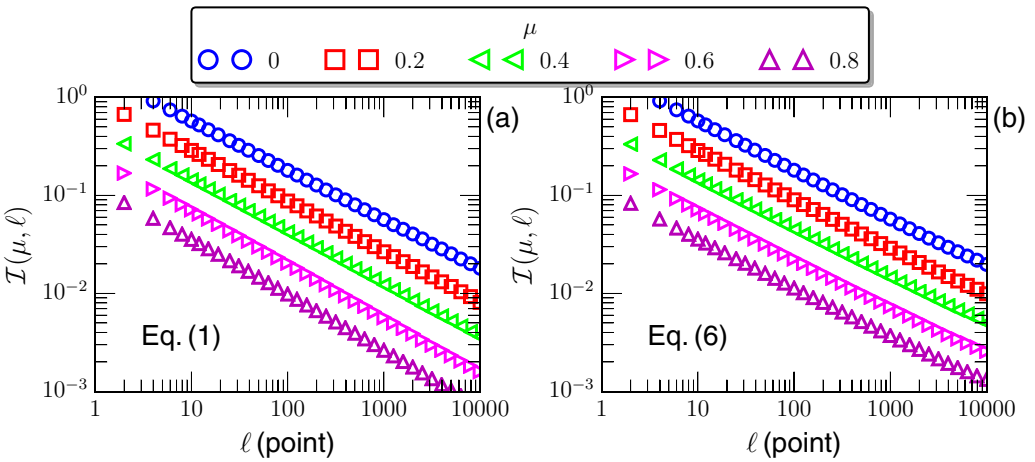

FIG. 14. $\mathcal{I}(\mu,\ell)$ versus ℓ from (a) direct counting and (b) Eq. (6). For display clarity, the curves have been vertical shifted. The corresponding scaling exponent $\xi(\mu)$ is fitted in the range $100 \leqslant \ell \leqslant 1000$.

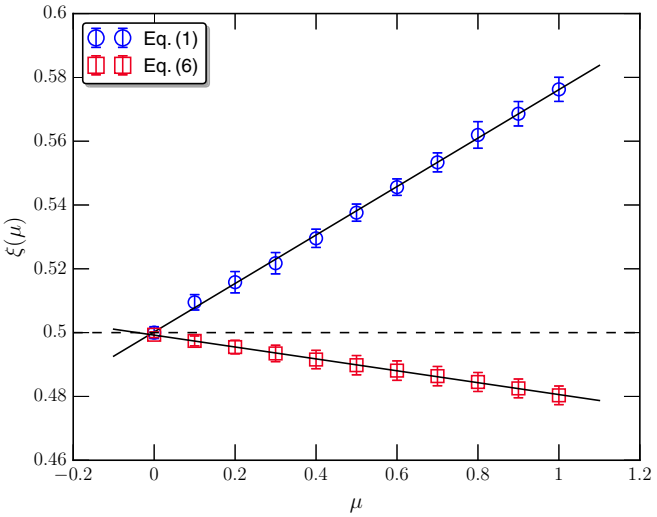

FIG. 15. Scaling exponent $\xi(\mu)$ versus μ from (a) direct counting (◯), and (b) Eq. (6) (□), where a linear fitting is illustrated by a solid line. The horizontal dashed line indicates the value 1/2 for Brownian motion.

Figure 8 shows a synthesized MRW time series $x_\mu(t)$, with various intermittency parameter μ and the data length $L = 2^{17}$. Similarly as for fBm, in the synthesized algorithm the same random numbers are used to construct the multifractal measure $\epsilon_\mu(t)$ for comparison. Visually, all these curves have a similar trend, while the relative variation increases with μ. The measured $\mathcal{I}(\mu) = 1/2$ is independent of μ, showing that the intermittency correction does not change the distribution of extremal points but changes the amplitude.

2. Structure-function scaling

The important feature of MRW can be understood from the structure function scaling. Conventionally the qth order structure function is defined as

$$S_q(\tau) = \langle |\Delta x_{\mu,\tau}(t)|^q \rangle \propto \tau^{\zeta(\mu,q)}, \tag{25}$$

where $\Delta x_{\mu,\tau}(t) = x_\mu(t+\tau) - x_\mu(t)$ is the increment, τ is the separation scale, and μ is the intermittency parameter ($0 \leqslant \mu \leqslant 1$) characterizing the lognormal cascade [32]. With the lognormal $\epsilon_\mu(t)$, the scaling exponent $\zeta(\mu,q)$ can be expressed as

$$\zeta(\mu,q) = \frac{q}{2} - \frac{\mu}{2}\left(\frac{q^2}{4} - \frac{q}{2}\right), \tag{26}$$

which previously has been verified for the $\mu = 0.15$ case by Huang *et al.* [33] and Huang [34].

The qth-order structure function $S_q(\tau)$ results from an ensemble average over 100 MRW realizations with $p = 17$, i.e., 131,072 data points. The power-law behavior is observed for all different μ (not shown here), based on which the scaling exponent $\zeta(\mu,q)$ can be estimated in the range $100 \leqslant \tau \leqslant 10\,000$. Figure 9 shows the contour plot of the relative error between the measured $\zeta(\mu,q)$ and the lognormal formula in Eq. (26). Visually, except for the upper-right corner, the relative error is below 5%, verifying MRW as expected for a broad range of parameter μ. Note that for the classical Eulerian turbulent velocity, a typical intermittency parameter is found in the range $0.2 \leqslant \mu \leqslant 0.4$ [35], see page 165. Despite the Hurst number difference (1/3 for the Eulerian velocity and 1/2 for MRW here), the MRW model produces the same intermittency correction.

3. Extremal-point-density statistics

Figure 10(a) shows $\mathcal{I}(\mu)$ from direct counting (◯) and Eq. (6) (□), Fig. 10(b) shows the measured relative error for $\mathcal{I}(\mu)$ and the standard deviation obtained from 100 realizations, which is shown as error bar in Fig. 10(a). There is an overestimation from Eq. (6). The relative error $\mathrm{Er}(\mu)$ increases with μ from 0% up to 2%, and the corresponding standard deviation increases from 0% up to 4%, which can be ascribed to the violation of the joint Gaussian distribution. As demonstrated in Fig. 11, except for the Brownian motion case with $\mu = 0$, the measured pdfs of $x'_\mu(t)$, the first-order derivative of $x_\mu(t)$, are far from the normal distribution.

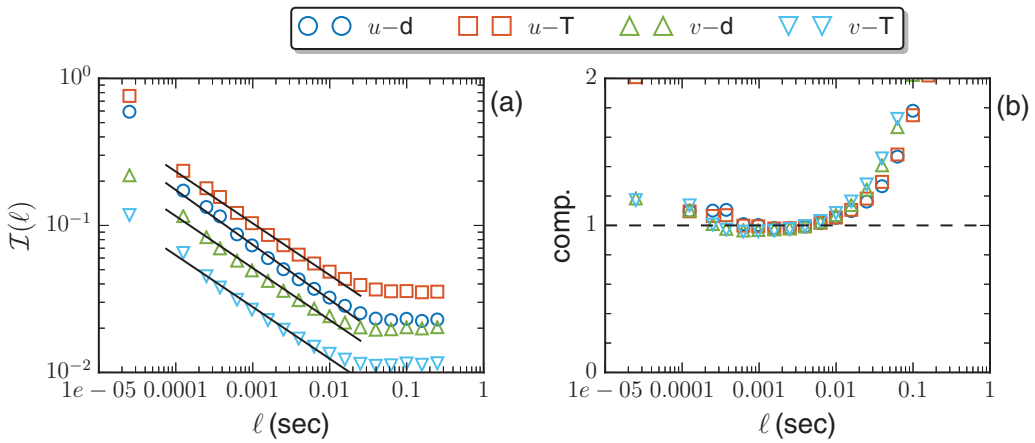

FIG. 16. (a) Measured $\mathcal{I}_H(\ell)$ for the turbulent velocity obtained from a wind tunnel experiment [36] with a Reynolds number $\mathrm{Re}_\lambda \simeq 720$. For display clarity, the curve for $u - \mathrm{T}$ and $v - \mathrm{T}$ have been vertically shifted by multiplying 1.5 and 0.5, respectively. The solid line is the power-law fit in the range $0.0001 \leqslant \tau \leqslant 0.01$ s, corresponding to a frequency in the range $100 < f < 10\,000$ Hz. (b) The corresponding curves compensated by the fitting parameters.

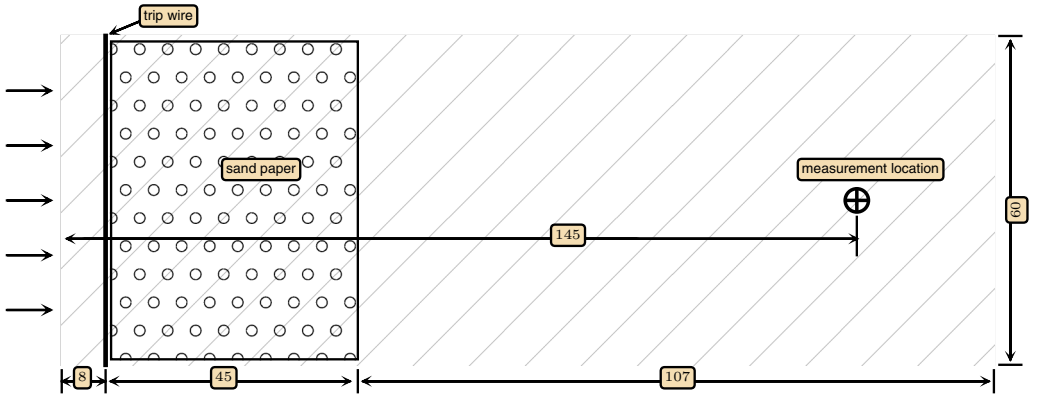

FIG. 17. Schematic representation of the boundary layer experimental setup [40] with a unit cm. The inflow is 4.5 ms^{-1} with a Reynolds number $\mathrm{Re}_\theta \simeq 810$. A trip-wire with a twisted-wire is located at 8 cm downstream to accelerate the turbulent boundary layer development. The measurement is performed at 145 cm downstream ($\oplus$).

Moreover, the tail part of the pdf increases with μ, implying a stronger intermittency when μ is larger.

4. Coarse-grained effect

Figure 12 shows $\mathcal{I}(\mu,\ell)$ versus μ at several ℓ from (a) direct counting and (b) Eq. (6). The following exponential-law behavior is observed:

$$\mathcal{I}(\mu,\ell) \propto e^{\pi(\ell)\mu}, \tag{27}$$

where $\pi(\ell)$ is a ℓ-dependent scaling exponent. Visually, two approaches provide opposite trends. More precisely, the result from direct counting predicts an exponential decay with μ, while the second estimator provides an exponential growing.

Figure 13(a) shows the $\pi(\ell)$ calculated by direct counting (Eq. (1), ◯) and Eq. (6) (□), confirming the observation in Fig. 12. Moreover, the intensity (absolute value) of scaling exponents $\pi(\ell)$ by Eq. (6) is much smaller than the one by direct counting for large values ℓ. Figure 13(b) shows a contour plot of the measured ratio $\mathcal{I}_\mathrm{T}(\mu,\ell)/\mathcal{I}(\mu,\ell)$, showing that Eq. (6) overestimates $\mathcal{I}(\mu,\ell)$ more when ℓ and μ increase.

Figure 14 presents the measured EPD for various μ from (a) direct counting and (b) Eq.(6), where for display clarity the curves have been vertical shifted. A power-law behavior is observed for all μ. The scaling exponent $\xi(\mu)$ is estimated in the range $100 \leqslant \ell \leqslant 1000$.

Figure 15 shows the measured $\xi(\mu)$ versus the intermittency parameter, μ. Using direct counting the measured $\xi(\mu)$ increases linearly with μ with a slope $\simeq$0.08, while due to the violation of the joint Gaussian distribution condition, the measured $\xi_\mathrm{T}(\mu)$ by Eq. (6) decreases linearly with μ with a slope $\simeq -0.02$.

According to the obtained results, it is meaningful to comment on the scaling exponent ξ. For a monofractal process, the measured ξ is found to equal to the Hurst number; or in other words, Eq. (22) provides a new idea to estimate the Hurst number. For a scaling process with intermittency correction, as shown in this work, ξ could also be influenced by the process intermittency, where Eq. (6) overestimates $\mathcal{I}_\mathrm{T}$, but underestimates ξ.

III. APPLICATIONS IN TURBULENT SYSTEMS

A. Eulerian turbulent velocity in wind tunnel

First, we consider here a velocity database obtained from a wind tunnel experiment with the Taylor scale λ-based Reynolds number $\mathrm{Re}_\lambda \simeq 720$ [36]. A probe array with four X-type hot wire anemometry were placed in the middle height and along the center line of the wind tunnel to record the velocity with a sampling frequency of 40 kHz at the streamwise direction $x/M = 20$, where M is the size of the active grid. The measure time is 30 s with 30 times repetition, i.e., totally

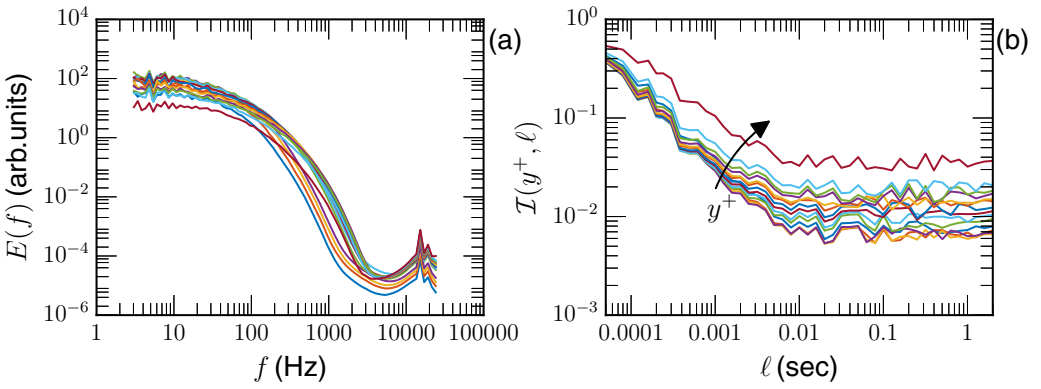

FIG. 18. (a) Measured Fourier power spectrum at different height y^+. (b) The corresponding $\mathcal{I}(y^+,\ell)$ versus τ.

there are $30 \times 4 \times 30 \times (40 \times 10^3)$ data points. The Fourier power spectrum $E_u(k)$ of the longitudinal velocity reveals a nearly two decades inertial range in the frequency range $10 \leqslant f \leqslant 1000\,\mathrm{Hz}$ (i.e., the time scale $0.001 < \tau < 0.1\,\mathrm{s}$) with a scaling exponent $\beta \simeq 1.65 \pm 0.02$. More details about this database can be found in Ref. [36]. Particularly the Taylor's frozen hypothesis [35] is not implemented here to convert the results into the spatial coordinate.

Figure 16(a) shows the measured EPD for both longitudinal u and transverse v velocity components via direct counting (denoted as d) and Eq. (6) (denoted as T). For display convenience, the curves have been vertically shifted. A clear power-law behavior exists in the range $0.0001 \leqslant \tau \leqslant 0.01\,\mathrm{s}$, corresponding to a frequency range $100 \leqslant f \leqslant 10\,000\,\mathrm{Hz}$. Note that the scaling range here is different from the one predicted by the Fourier power spectrum since the coarse-grained operator has been applied to measure $\mathcal{I}(\ell)$ [37]. It is found that $\xi = 0.37 \pm 0.01$ for the u-d and 0.35 ± 0.01 for the rest. Interestingly for the same database the 0.37 scaling has been observed from the velocity increment pdf [38], which also agrees with the first-order structure function scaling for high Reynolds number turbulent flows [39].

B. Eulerian velocity in turbulent boundary layer

Another turbulent data analyzed here is the Eulerian velocity from a zero-pressure-gradient turbulent boundary layer experiment [40]. We recall briefly the main relevant parameters. As shown in the experiment schematic Fig. 17, to achieve a fully developed boundary layer structure, a trip wire with diameter 2 mm was placed at 8 cm after the leading edge, followed with a 45 cm in length sand paper. The inflow speed is $4.5\,\mathrm{ms}^{-1}$ and the measurement was performed at 145 cm downstream. The corresponding momentum thickness θ based Reynolds number is $\mathrm{Re}_\theta \simeq 810$. A commercial hot-wire was operated in constant-temperature anemometry mode by TSI-IFA300 unit. The signals were sampled during ~84 s at frequency $f_s = 50\,\mathrm{kHz}$ with a low-pass at a frequency of 25 kHz. We consider only the longitudinal velocity.

Figure 18(a) shows the measured Fourier power spectrum $E(f)$ at different height y^+, where the cutoff frequency is roughly around $f_N = 3{,}000\,\mathrm{Hz}$, above which the data is dominated by noise. Due to the finite Reynolds number, no clear power-law behavior can be observed. Figure 18(b) shows the measured $\mathcal{I}(y^+,\ell)$ versus ℓ. By contrast the power-law can be observed roughly when $\ell \leqslant 0.01\,\mathrm{s}$, which, however, could be due to the measurement noise. The measured $\mathcal{I}(y^+,\ell)$ decreases rapidly with ℓ and becomes saturated when $\ell \gg 0.01\,\mathrm{s}$. For a fixed ℓ, $\mathcal{I}(y^+,\ell)$ seems to increase with y^+.

We then reproduce the measured $\mathcal{I}(y^+,\ell)$ versus y^+ in Fig. 19. Different sublayer regions inside the boundary layer are marked by vertical lines, which are the viscous sublayer with $y^+ \leqslant 5$, the buffer layer with $5 \leqslant y^+ \leqslant 30$, the log-law region with $30 \leqslant y^+ \leqslant 200$, and the outer layer $y^+ > 200$, respectively. Interestingly, the measured EPD for large value of ℓ shows four different regimes as well, coincidentally in agreement with the four different sublayer regions. Therefore it is reasonable to claim that the proposed EPD analysis can be effective to detect the boundary layer structure. Additionally the inverse of EPD, $\mathcal{I}^{-1}(y^+,\ell)$, roughly measures an average scale of turbulent structures. Therefore, small value of $\mathcal{I}(y^+,\ell)$ indicates some well-organized large-scale structure.

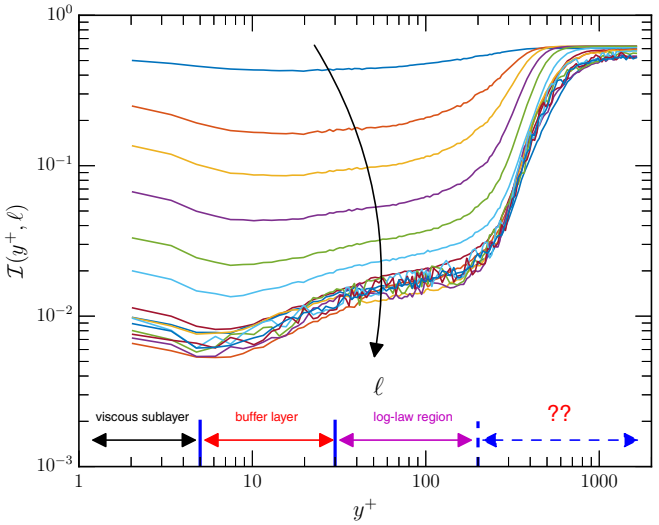

FIG. 19. The measured EPD $\mathcal{I}(y^+,\tau)$ versus y^+ reproduced in a log-log view, together with the four regimes of the turbulent boundary layer structure.

IV. CONCLUSIONS

In summary, EPD of several typical scaling time series has been investigated. The fBm result agrees with the the theoretical prediction by Toroczkai *et al.* [13] [Eqs. (6) or (9)] since the process satisfies the Gaussian condition of the joint distribution of the correlation coefficients. When the Hurst number $H \leqslant 0.6$, the measured EPD agrees with Eq. (16), but deviates when $H > 0.6$. Using a coarse-grained operator the measured scaling exponent $\xi(H)$ is found to equal to H, providing a new idea to estimate the Hurst number. Due to the nondifferentiable property of the fBm process, EPD predicted by the Rice's formula is largely different from the direct counting result. For multifractal random walk with lognormal statistics, EPD via direct counting is independent of the intermittency parameter μ, suggesting that the intermittency effect may not change the distribution of the extremal points, but changes the amplitude. Due to the intermittency correction, Eq. (6) overestimates EPD systematically, due to the violation of the joint Gaussian distribution condition. After the coarse-grained operation, the power-law behavior is still preserved. The result from direct counting suggests that $\xi(\mu)$ increases linearly with μ; differently $\xi(\mu)$ from Eq. (6) decreases linearly with μ.

The EPD analysis was then applied to the experimental turbulent velocity data from wind tunnel flow with $\mathrm{Re}_\lambda \simeq 720$ and a turbulent boundary layer with $\mathrm{Re}_\theta \simeq 810$. For the former case, the scaling exponent ξ for the longitudinal velocity is $\xi \simeq 0.37$, which is in agreement with the value from the conventional first-order structure function analysis via the extended self-similarity technique [39]. For the latter case, the measured EPD after the coarse-grained operation shows clearly four regimes, which coincides with the classical turbulent boundary layer structure, including the viscous sublayer, buffer layer,

log-law region, and the outer layer. A high-order dimension (respectively, 2D and 3D) extension of this approach for PIV (particle image velocimetry) measurements or high resolution DNS (direct numerical simulation) is under progress, and will be shown elsewhere.

ACKNOWLEDGMENTS

This work is sponsored by the National Natural Science Foundation of China (under Grants No. 11332006 and No. 91441116), and partially by the Sino-French (NSFC-CNRS) joint research project (No. 11611130099, NSFC China, and PRC 2016-2018 LATUMAR "Turbulence lagrangienne: études numériques et applications environnementales marines," CNRS, France). Y.H. is also supported by the Fundamental Research Funds for the Central Universities (Grant No. 20720150075). We thank Prof. Meneveau at Johns Hopkins University for providing us the experiment data, which can be found at Ref. [41]. A MATLAB source package to realize the Extremal-Point-Density analysis is available at Ref. [42]. Useful comments by a referee are gratefully acknowledged.

[1] A. N. Kolmogorov, Dokl. Akad. Nauk SSSR **30**, 301 (1941).
[2] J. F. Muzy, E. Bacry, and A. Arneodo, Phys. Rev. E **47**, 875 (1993).
[3] B. Lashermes, S. Jaffard, and P. Abry, *Proceedings of the ICASSP 2005 Conference, Philadelphia, PA* (IEEE, 2005).
[4] N. E. Huang, Z. Shen, S. Long, M. Wu, H. Shih, Q. Zheng, N. Yen, C. Tung, and H. Liu, Proc. R. Soc. London, Ser. A **454**, 903 (1998).
[5] Y. Huang, F. G. Schmitt, Z. Lu, and Y. Liu, Europhys. Lett. **84**, 40010 (2008).
[6] L. P. Wang and Y. X. Huang, J. Stat. Mech.: Theor. Exp. (2015) P06018.
[7] F. G. Schmitt and Y. Huang, *Stochastic Analysis of Scaling Time Series: From Turbulence Theory to Applications* (Cambridge University Press, Cambridge, 2015).
[8] Y. Huang, F. G. Schmitt, Z. Lu, P. Fougairolles, Y. Gagne, and Y. Liu, Phys. Rev. E **82**, 026319 (2010).
[9] S. O. Rice, Bell Syst. Tech. J. **23**, 282 (1944).
[10] M. R. Leadbetter, G. Lindgren, and H. Rootzén, *Extremes and Related Properties of Random Sequences and Processes* (Springer Science & Business Media, Berlin, 2012).
[11] M. S. Longuet-Higgins, Proc. R. Soc. Lond. **246**, 99 (1958).
[12] N. D. Ylvisaker, Ann. Math. Stat. **36**, 1043 (1965).
[13] Z. Toroczkai, G. Korniss, S. DasSarma, and R. K. P. Zia, Phys. Rev. E **62**, 276 (2000).
[14] H. W. Liepmann, Helv. Phys. Acta **22**, 119 (1949).
[15] K. R. Sreenivasan, A. Prabhu, and R. Narasimha, J. Fluid Mech. **137**, 251 (1983).
[16] P. Kailasnath and K. R. Sreenivasan, Phys. Fluids **5**, 2879 (1993).
[17] C.-M. Ho and Y. Zohar, J. Fluid Mech. **352**, 135 (1997).
[18] D. Poggi and G. G. Katul, Phys. Fluids **21**, 065103 (2009).
[19] D. Poggi and G. G. Katul, Bound. Lay. Meteorol. **136**, 219 (2010).
[20] D. Cava, G. G. Katul, A. Molini, and C. Elefante, J. Geophys. Res. **117** (2012).
[21] K. Yang, Z. Xia, Y. Shi, and S. Chen, Commun. Comput. Phys. **19**, 251 (2016).
[22] A. N. Kolmogorov, Dokl. Akad. Nauk SSSR **26**, 115 (1940).
[23] B. Mandelbrot and J. Van Ness, SIAM Rev. **10**, 422 (1968).
[24] J. Beran, *Statistics for Long-memory Processes* (CRC Press, Boca Raton, FL, 1994).
[25] L. Rogers, Math. Finance **7**, 95 (1997).
[26] P. Doukhan, M. Taqqu, and G. Oppenheim, *Theory and Applications of Long-Range Dependence* (Birkhauser, Berlin, 2003).
[27] Y. Huang, F. G. Schmitt, Z. Lu, and Y. Liu, J. Hydrol. **373**, 103 (2009).
[28] A. T. A. Wood and G. Chan, J. Comput. Graph. Stat. **3**, 409 (1994).
[29] Y. Huang and F. G. Schmitt, J. Fluid Mech. **741**, R2 (2014).
[30] E. Bacry, J. Delour, and J. F. Muzy, Phys. Rev. E **64**, 026103 (2001).
[31] J. F. Muzy and E. Bacry, Phys. Rev. E **66**, 056121 (2002).
[32] F. G. Schmitt, Eur. Phys. J. B **34**, 85 (2003).
[33] Y. X. Huang, F. G. Schmitt, J.-P. Hermand, Y. Gagne, Z. M. Lu, and Y. L. Liu, Phys. Rev. E **84**, 016208 (2011).
[34] Y. Huang, J. Turbul. **15**, 209 (2014).
[35] U. Frisch, *Turbulence: the legacy of AN Kolmogorov* (Cambridge University Press, Cambridge, 1995).
[36] H. Kang, S. Chester, and C. Meneveau, J. Fluid Mech. **480**, 129 (2003).
[37] R. H. Kraichnan, J. Fluid Mech. **62**, 305 (1974).
[38] Y. Huang, F. G. Schmitt, Q. Zhou, X. Qiu, X. Shang, Z. Lu, and Y. Liu, Phys. Fluids **23**, 125101 (2011).
[39] R. Benzi, S. Ciliberto, R. Tripiccione, C. Baudet, F. Massaioli, and S. Succi, Phys. Rev. E **48**, R29 (1993).
[40] X.B. Zheng and N. Jiang, Chin. Phys. B **24**, 064702 (2015).
[41] http://turbulence.pha.jhu.edu/.
[42] https://github.com/lanlankai.